Journal of Solid State Electrochemistry
https://doi.org/10.1007/s10008-024-05892-9

ORIGINAL PAPER

Influence of nano-crystallization on Li-ion conductivity in glass Li_3PS_4: a molecular dynamics study

Kobayashi Ryo[1,3] · **Takemoto Seiji**[2] · **Ito Ryuichiro**[1,2]

Received: 4 March 2024 / Revised: 4 April 2024 / Accepted: 4 April 2024

Abstract
Understanding the ionic conduction mechanisms in solid electrolyte glasses and glass-ceramics is an important task for improving the performance of next-generation all-solid-state batteries. Although many ionic conduction mechanisms have been proposed, the mechanism of increased ionic conductivity in partially crystallized glass is not fully understood. In this study, molecular dynamics was used to analyze the strain and local ion mobility in the glass around the crystal nano-particles of Li_3PS_4, which is a promising material for solid electrolytes. From the analysis of the results, we find that a local strain field is generated around the crystal particles and that the tensile strain field decreases the activation energy of ion migration and increases the ionic conductivity. This study opens the possibility of improving the ionic conductivity of glass-ceramics by controlling crystallization and dispersing the tensile strain field, even though the crystalline phase is not a high ionic conducting phase.

Keywords Solid electrolyte · Lithium thiophosphate · Li-ion battery · Molecular dynamics

Introduction

All-solid-state batteries which utilize solid electrolytes (SEs) are thought to be the next-generation Li-ion batteries (LIBs), owing to its superior qualities over conventional LIBs including heat resistance, non-flammability, and high energy density [1, 2]. High ionic conductivity and high formability are two of the SE's key characteristics that enable fast charging/discharging with improved contact with active materials [3]. Since certain sulfide material classes meet these criteria, lithium sulfide materials are regarded as promising candidates for SEs. Because of its excellent formability and the presence of highly ionic-conductive crystalline and glass phases, the lithium phosphorus sulfide $x\mathrm{Li_2S}$-$y\mathrm{P_2S_5}$ with $x : y = 3 : 1$ ($\mathrm{Li_3PS_4}$) is thought to be one of the most promising among the sulfide materials [4, 5].

Many investigations have been carried out in an effort to identify and stabilize higher ion-conductive phases in Li_3PS_4 [6, 7]. Ionic conductivity is typically higher in glass phases (10^{-4} to 10^{-3} S cm^{-1}) compared to crystalline phases [4, 8]. In particular, γ-Li_3PS_4, which is thermodynamically stable at room temperature (RT), has low ionic conductivity ($\sim 10^{-7}$ S cm^{-1}) [6]. In contrast, there exists a super ionic-conductive phase, α-Li_3PS_4 ($> 1 \times 10^{-3}$ S cm^{-1}) [9], and glass-ceramics containing α-phases embedded in the glass through crystallization are known to have conductivity higher than the glass phase [10]. However, for glass-ceramics with extremely low crystallinity of low ionic conductivity phase, an increase in ionic conductivity was also discovered [11]. Therefore, it appears that there are other factors contributing to the rise in ionic conductivity in glass-ceramics besides the percolation of highly conductive α-phase.

Due to their inherent lack of periodic ordering, the ion-conduction mechanisms of glass and glass-ceramics are thought to be extremely complex in comparison to crystalline

✉ Kobayashi Ryo
kobayashi.ryo@nitech.ac.jp

Takemoto Seiji
seiji.takemoto@murata.com

Ito Ryuichiro
ryuichiro.ito@murata.com

[1] Department of Applied Physics, Nagoya Institute of Technology, Gokiso-cho, Showa-ku, Nagoya, Aichi 466-8555, Japan

[2] Murata Manufacturing Co., Ltd., 1-10-1, Higashikotari, Nagaokakyo, Kyoto 617-8555, Japan

[3] Department of Carbon Neutrality Science and Engineering, Nagoya Institute of Technology, Gokiso-cho, Showa-ku, Nagoya, Aichi 466-8555, Japan

Published online: 12 April 2024

phases. As a result, numerous mechanisms have been proposed and examined. Many researchers have discussed the significance of local structures like the S-sublattice, which is a key distinction between glassy and crystalline structures [9, 12, 13], poly-anion blocks like PS_4^{3-}, $P_2S_6^{4-}$, and $P_2S_7^{4-}$, which are also typical of glasses [4, 5, 14], charge polarization around Li-ions depending on the local environment [15], and glass density, which varies depending on the process conditions among samples [8, 16]. Additionally, whether or not the rotating poly-anions improve Li-ion migration has been studied in relation to dynamical properties like the paddle-wheel mechanism [17–20]. Despite numerous attempts, the increase of ionic conductivity in glass-ceramics through crystallization has not yet been fully understood, because of the difficulty in analyzing amorphous structures and the interface between glass and crystal phases.

The molecular dynamics (MD) method is deemed appropriate for investigating Li-ion conduction within the glass phase and at the interface between glass and crystal. Kim et al. [12] conducted MD simulations of a system with γ-crystal and glass side-by-side using a classical interatomic potential (IP). They showed that Li-ion conductivity at the interface is an intermediate value between those of γ-phase and glass, which they attributed to a combination of S-sublattice features from both phases. Shimuzu et al. [21] performed a long-time MD simulation using a machine-learning (ML) IP of annealing from a glass phase. They showed that under a certain temperature high ionic-conductive α-like phase nucleates and claimed that the increase of Li-ion conductivity of glass-ceramics is due to percolation of the high ionic-conductive crystalline phase. However, these studies do not explain the mechanism of the increase of ionic conductivity of glass-ceramics under low crystallinity [11], probably because they have not taken into account the change of glass phase due to crystal nucleation, particularly the glasses' density as discussed in Ref. [16].

In this study, we perform comprehensive MD simulations to examine the variations in glass density surrounding the nano-crystal in Li_3PS_4 glass-ceramics and we carry out non-equilibrium MD (NEMD) simulation to investigate the local ion mobility both inside and outside the nano-crystal, using a newly developed IP for Li_3PS_4 system by learning dynamical properties from *ab-initio* calculations. Based on the analysis of the data, we can conclude that there is a tensile strain field surrounding the nano-crystal and that this strain field increases the Li-ion conductivity in glass-ceramic Li_3PS_4.

Results and discussion

Interatomic potential (IP) for Li_3PS_4

The IP function forms are outlined in the "Interatomic potential (IP) function form'' section. The Cuckoo search algorithm [22] and the autonomous search space update method [23] were used to optimize the potential parameters. *Ab-initio* MD (AIMD) calculations were used to obtain selected target data for the optimization. These calculations included the energy vs. volume relationship, mean squared displacements of Li-ions, phonon density of states, radial and angular distribution functions (RDF and ADF) of α, β, and γ structures at 700 K, and energy differences between α and glass structures obtained via MD simulation using the potential with a trial parameter set. Therefore, the present IP well reproduces the dynamical properties of Li_3PS_4.

Li-ion conductivities obtained by the current IP for α, β, and γ Li_3PS_4 are shown in Fig. 1(a), where they are compared to those obtained by a machine-learning (ML) IP in Ref. [20]. Although the conductivities are underestimated in the current IP, the temperature dependence of conductivities of the α and γ phases is accurately reproduced. In contrast to the MLIP, which shows that the conductivity of the β phase is considerably lower than that of the α phase, the current

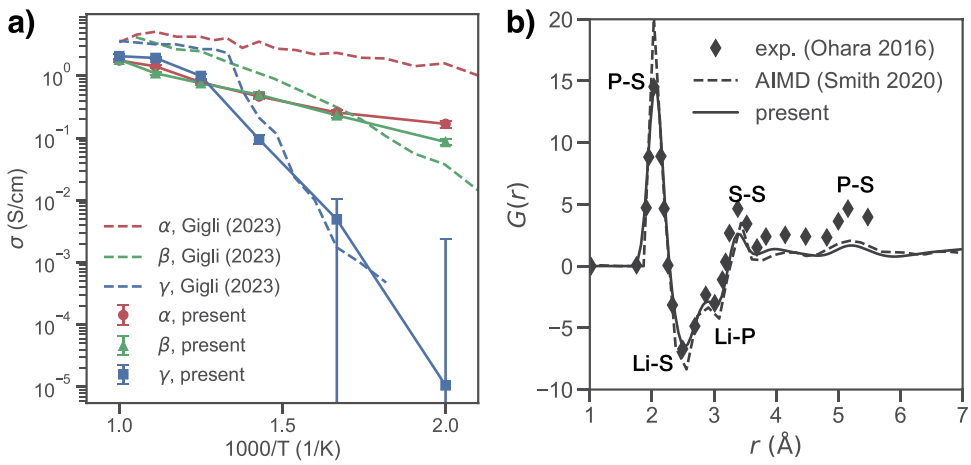

Fig. 1 **a** Li-ion conductivities of α (red), β (green), and γ Li_3PS_4 (blue) obtained by the present IP and by a machine-learning potential from Ref. [20]. **b** Pair distribution functions $G(r)$ of glass structures obtained from the present IP, AIMD [19] and experiment [4] whose data points were extracted from [19]

IP predicts that the conductivity of the β phase is about the same as that of the α phase as seen in Fig. 1(a). This suggests that the current IP's prediction for the β phase is not accurate enough to be compared with the other phases.

Figure 1(b) shows the pair distribution function, $G(r)$, computed using a bulk glass model obtained using the present IP, comparing with previous experimental and AIMD studies. This demonstrates that the glass structure created using the present IP reproduces well what is obtained by experiments and ab-initio calculations. Furthermore, the activation energy of the glass phase is 0.30 eV and the estimated ion conductivity of glass at RT is approximately 1.0×10^{-3} S cm^{-1} (as shown Fig. 6c), which is in good agreement with previous studies. Therefore, the current IP is thought to be appropriate for this study because we concentrate on the Li-ion conduction in glass, embedded γ phase, and their interface. Note that this IP includes a penalty to the formation of clusters between PS_4^{3-} units which may not be realistic since other poly-anion building blocks such as $P_2S_6^{4-}$ and $P_2S_7^{4-}$ were considered to exist in Li_3PS_4 glasses [4, 5]. However, since a recent study suggested that the effect of these poly-anions on the ionic conductivity is not so significant as other contributions such as density [16], using the current IP we eliminate the poly-anion effects and examine only the contributions of density and other local structures. Parameter values and other bulk properties of the current IP are shown in Supplementary Information.

Structure of partly crystallized glass-Li_3PS_4

We created a simulation model of glass-Li_3PS_4 containing a γ-Li_3PS_4 nano-particle at the center of the simulation cell by the process described in "Construction of glass-ceramics model'' section. In this investigation, we selected the γ-phase as a nano-particle inside glass because it is the most stable structure in the Li_3PS_4 composition at RT and it has a higher density than β, α, and glass phases, which helps to highlight the influence of dense phase nano-crystallization. The system is a periodic cell with this is nearly cubic, with each edge spanning approximately 180 Å, and containing a total of 288,144 ions. Figure 2(a) depicts the evolution of temperature and pressure during the annealing, quenching, and equilibrating stages. During the model preparation except for the equilibrating stage, we forced P-S bonds in PS_4 unit not to break by setting spring beads potential so that poly-anion blocks other than PS_4 would not appear during the fast annealing of rather a high temperature which is not

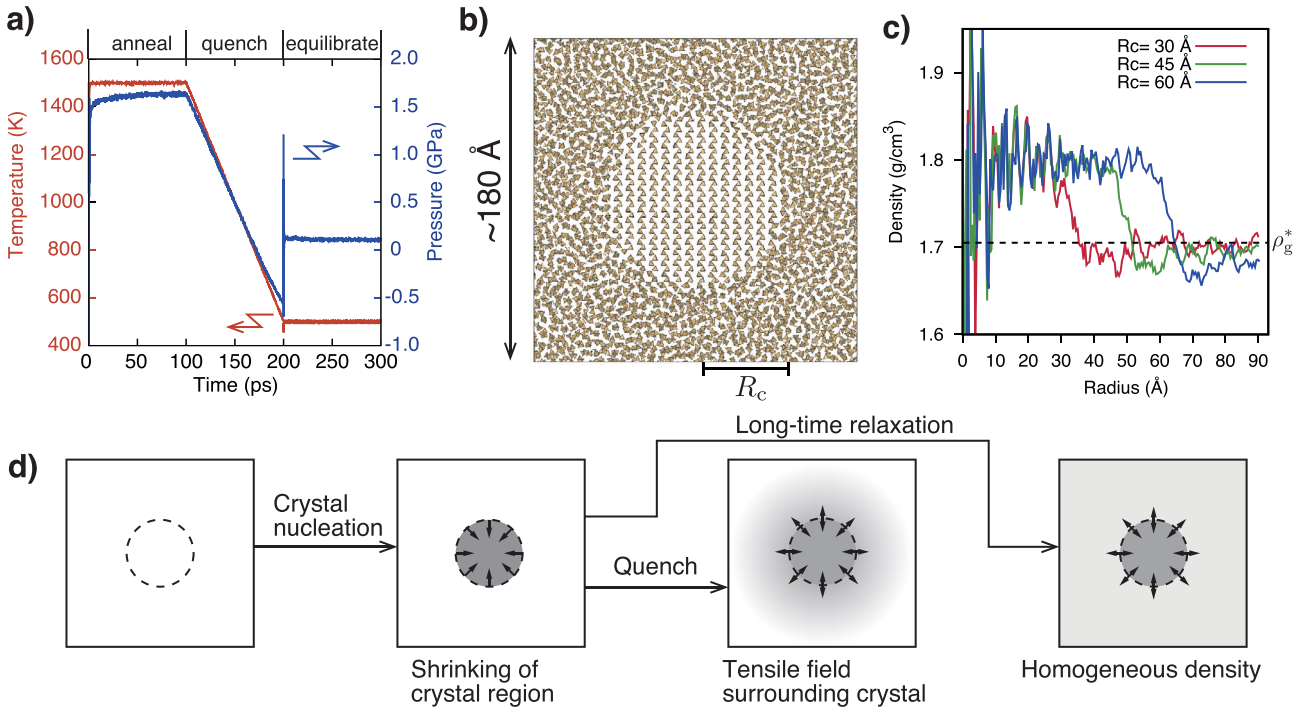

Fig. 2 **a** Temperature and pressure evolution during the production of glass-ceramic model. The spike appeared at 200 ps because the potential was changed from the spring potential for neighboring P-S bonds to the Morse potential. **b** Sliced cross-section of the glass-ceramic structure after equilibration. R_c is the radius of γ-Li_3PS_4 in the glass-ceramic model. Only PS_4 polygons are shown. **c** Densities of glass-ceramic models with $R_c = 30, 45, 60$ Å as a function of radius from the center. Equilibrium glass density, ρ_g^* is shown as a dashed line. **d** Scenario of tensile strain field in the surrounding glass matrix after crystal nucleation

a realistic situation. By applying this restriction, we eliminate the contribution of poly-anion blocks such as $P_2S_6^{4-}$ and $P_2S_7^{4-}$ and focus only on density and local structures. Since the system's density was maintained throughout the entire process, the pressure increased by more than 1 GPa during the annealing phase which is higher than the pressure (460 MPa) applied to densify the glass to eliminate voids from pellets [8], and the resulting glass structure may have unique characteristics as a result of the pressure history. Nonetheless, as the temperature and pressure histories are identical for every case used for comparison in this study, the impact would not be felt in the discussion that follows.

The cross-section of the glass-ceramic system containing a nano-crystal of radius $R_c = 45$ Å is displayed in Fig. 2(b), with only the PS_4 polygons displayed for ease of distinguishing between the crystalline and glass regions. The cross-section is sliced at the plane that includes the system's center. The nano-crystal had some tiny facets at the glass-crystal interface after it had equilibrated, but other than that, it nearly retained its spherical shape and crystalline structure, neither growing nor shrinking, even after a 1-ns equilibration period at 500 K. We have also examined the shape and facets of α -phase nano-crystal of $R_c = 45$ Å after the equilibration, and the above conclusion also applies the α nano-crystal.

The presence of a high-density nano-crystal inside a fixed density of glass affected the glass structure surrounding the nano-crystal. The local densities of three distinct cases of nano-crystals, $R_c = 30$, 45, and 60 Å, are displayed in Fig. 2(c) as a function of radius R from the nano-crystal center. Density at radius R was computed by the weights of ions inside a shell from $R - \Delta R/2$ to $R + \Delta R/2$ divided by the shell volume $4\pi R^2 \Delta R$. The density drops from about 1.8 g/cm^3 to below the equilibrium glass density, $\rho_g^* = 1.705$ g/cm^3 at 500 K, when the R exceeds the radius of the nano-crystal. The radius of the nano-crystal determines the glass-part density; the larger the nano-crystal, the less dense the glass. This makes sense because the system's overall density was fixed from annealing to equilibration. This suggests that the size of the entire system under consideration as well as the duration of the structure relaxation process both affect the density of the glass component. It is possible, nevertheless, that the strain surrounding the nano-crystals will persist after quenching as illustrated in Fig. 2(d), resulting in an uneven strain field in the glass matrix and a shift in the Li-ion conduction of the glass matrix.

Ion mobility of glass surrounding nano-crystals

Local Li-ion mobility was computed from the ion flux obtained via NEMD at 500 K with an external force to drive Li-ions as described in the "Local ion flux analysis from non-equilibrium MD" section. In order to make the problem simpler, we considered a thin pseudo-two-dimensional system and an embedded cylindrical γ-phase at the system's center, as shown in Fig. 3. The yz area of the system matched that of the preceding 3D system, while its thickness along the x-axis was approximately 22 Å. The total ion count in the system was 37,584. The external force was applied parallel to the longitudinal direction of the cylinder. This cylindrical crystal configuration resembles a spherical nano-crystal in three dimensions, and it is thought that the influence of the nano-crystal embedding to the glass matrix is comparable in these two configurations. Three cases of different radii of nano-cylinders, 30, 45, and 60 Å, were considered corresponding to the preceding 3D models.

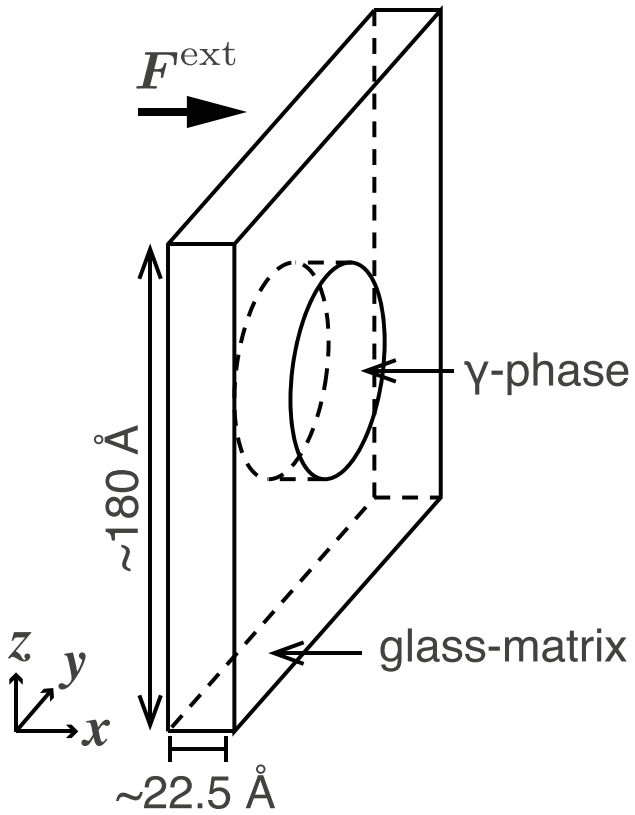

Fig. 3 Schematic diagram of the pseudo-2D glass-ceramic system used for the NEMD simulations

Heat maps of the local ion mobility in bulk glass and glass-ceramic ($R_c = 45$ Å) systems are shown in Fig. 4(a) and (b), respectively. There are high and low mobility regions without translational or rotational order in the glass region. As demonstrated in Fig. 1, the low ion conductivity of bulk γ phase is consistent with the mobility inside the γ region in Fig. 4(b), which is noticeably lower than that of the glass region. Certain regions (highlighted in red in Fig. 4b) at the interface between the glass and γ region exhibit a remarkably high ion mobility. However, it is unclear whether or not the ion mobility is enhanced at the

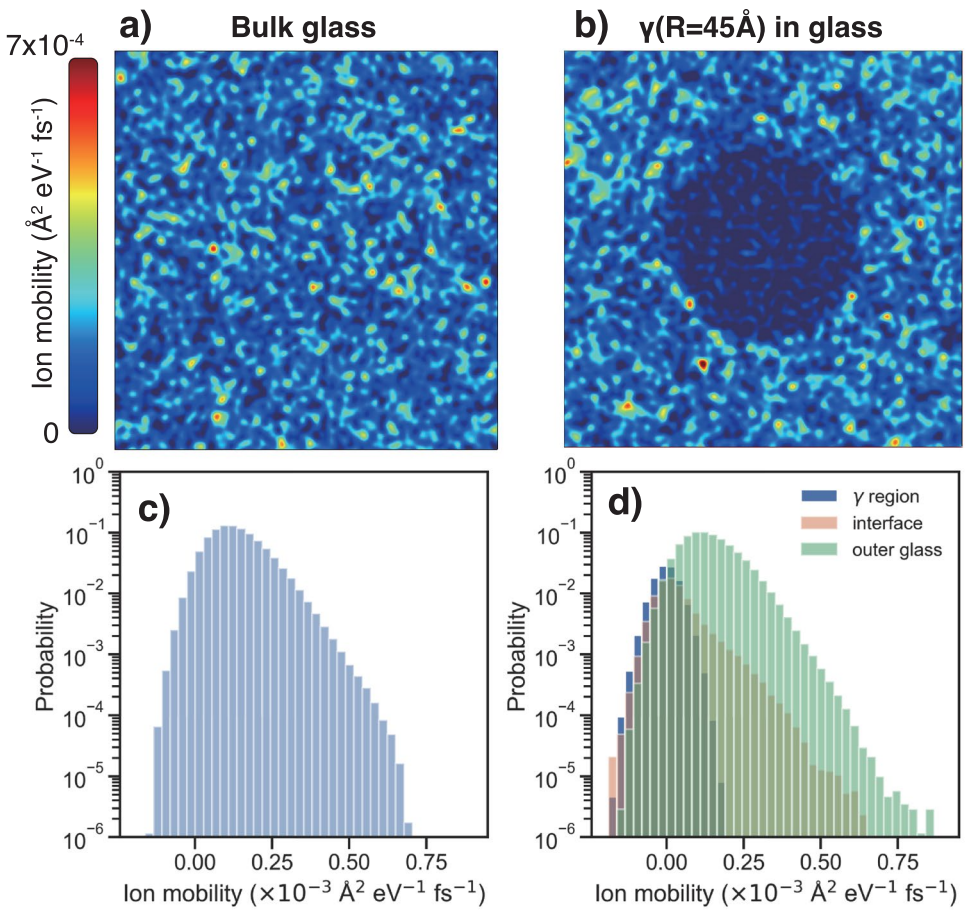

Fig. 4 Ion mobility in pseudo-2D bulk glass and glass-ceramic systems. **a**, **b** The distributions of local ion mobility in *yz* plane (normal to *x* and $\boldsymbol{F}^{\mathrm{ext}}$) in glass and glass-ceramic ($R_c = 45$ Å) systems, respectively. **c**, **d** The histograms of the local ion mobility in glass and glass-ceramic systems, respectively. The histogram is taken separately for inside γ region, interface, and outer glass region with the interface width of 15 Å for the glass-ceramic system

interface because there are also high mobility regions in the bulk glass in Fig. 4(a) and in the outer glass region of glass-ceramic system in Fig. 4(b). The local ion mobilities were also compared to the local ion densities of the corresponding cross-sections in Fig. S6, but no obvious correlation was observed between the two.

We computed histograms of ion mobility in the glass and glass-ceramic systems, as shown in Fig. 4(c) and (d), respectively, to investigate the differences in ion mobilities in these systems. We defined the interface as a region $R_c < R \le R_c + w$ and the surrounding glass region as $R > R_c + w$ with the radius R from the center and $w = 15$ Å. The glass system's histograms peak at approximately 1.0×10^{-4} Å^2 eV^{-1} fs^{-1}, while the glass-ceramic system's is slightly higher at about 1.25×10^{-4} Å^2 eV^{-1} fs^{-1}. Furthermore, the maximum mobility in the glass system in Fig. 4(c) is much smaller than in the glass-ceramic system in Fig. 4(d), suggesting that the nano-crystal nucleation in the glass has a notable impact on the surrounding glass's ion mobility.

Figure 5(a) shows the mean and standard deviation of ion mobility, indicating that even if averaging over the shell of a cylindrical surface, the difference between the bulk glass and glass-ceramic systems is not significant compared with their standard deviation. It further demonstrates that there is no discernible increase in ion mobility at the crystal/glass contact; instead, ion mobility is rather slightly higher in the outer glass region.

To clarify the change of ion mobility, it is required to take the averages in a wider area. Figure 5(b) plots the maximum and mean mobilities averaged over crystal and glass regions as a function of the radius of nano-crystal, R_c. Since the simulation cell volumes are the same for all cases and the surrounding glass area decreases as R_c increases, it makes sense that the total mean mobility decreases as the nano-crystal's radius increases in the systems. This corresponds to the decrease in ionic conductivity in the case of high crystallinity of low ion-conductive crystal phase observed in Ref. [11]. Conversely, as R_c increases, the mean and maximum mobilities in the surrounding glass regions increase (green and blue points in Fig. 5b). Since the contribution from the interface is not as large as that of the surrounding glass region as shown in Fig. 4(d) and is not included in the mean mobility of the glass region, the increase in ion mobility results from the existence of nano-crystals, which alter the properties of the glass and are primarily caused by tensile strain condition.

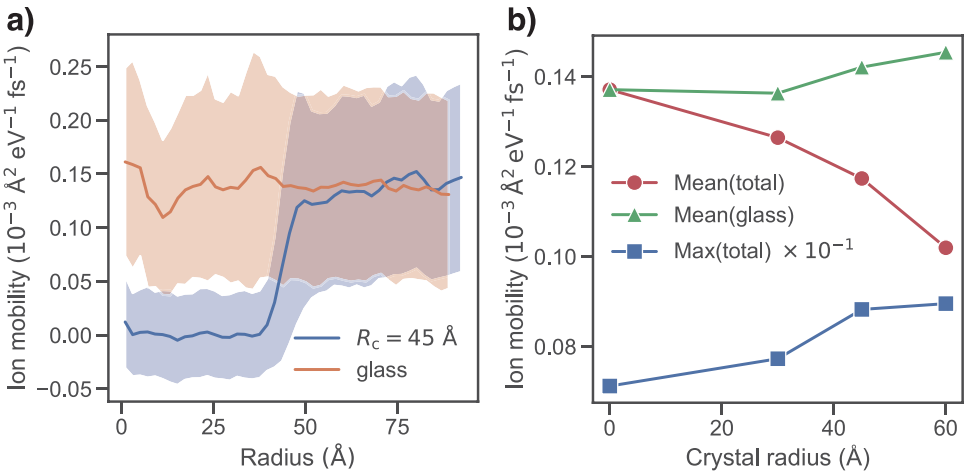

Fig. 5 **a** Ion mobilities of bulk glass and glass-ceramic systems as a function of radius from the cylinder center. Shaded area displays standard deviation of the ion mobility. **b** The mean ion mobilities of entire system and glass region, and the maximum local mobility of entire system as a function of crystal radius, R_c. Errors are not shown as they are three orders of magnitude smaller

Strain dependence of ion conductivity in Li_3PS_4 glass

In order to assess the strain dependence of Li-ion conductivity of glass-Li3PS4, we created 20 independent samples of bulk glass systems with 1024 ions using the same annealing, quenching, and equilibrating procedures as above with the exception that constant-stress ($N\sigma T$) MD with 1 GPa external pressure was carried out in the present case. We computed Li-ion diffusion coefficients, D's, for various isotropic strains at 500 K for each sample. Figure 6(a) shows the diffusion coefficients as a function of the density of the strained system. Consistent with the findings in the preceding section, the diffusion coefficient increases nearly linearly as the density decreases. This tendency is consistent across the board for the glass samples, as the error bars are sufficiently small with respect to the difference of D. The likely cause of the trend's violation at the lowest density ($< 1.5\,\mathrm{g/cm^3}$) is the appearance of a small void-like space in the system that does not contribute to Li-ion diffusion path.

The diffusion coefficient of the strained system is displayed as an Arrhenius plot in Fig. 6(b). In the present strained systems, all the cell vectors were deformed by plus or minus 2% which correspond to the densities of 1.6 and 1.8 $\mathrm{g/cm^3}$, respectively, in this case. Although the density change by these strains is considerably large as compared to the density decrease outside the nano-crystal in Fig. 2(c), we employed such large density modulations in order to clearly see the effect of glass density. Based on the slope of the lines, the activation energies E_a's for these strained systems are 0.39, 0.33, and 0.30 eV for -2%, 0%, and +2%, respectively. This indicates that the activation energy is reduced by tensile expansion by a maximum of 10%, which agrees well with an AIMD result [16]. We also investigated the prefactor of diffusion coefficients, D_0's, of these strained systems. Figure 6(c) shows the linear relationship between $\ln(D_0)$ and E_a, indicating that the Meyer-Neldel rule is valid for the strained glasses.

By using the activation energies, we calculated the Li-ion conductivity at lower temperatures, provided that the migration mechanism remains the same. Figure 6(d) compares the extrapolated conductivities and those of former studies from the literature. The estimated conductivity at RT is in good agreements with former experimental studies [4, 10, 11]. The present calculation underestimates the ion conductivities of AIMD calculations [16, 19] at RT. This is probably an issue of the current IP since it also underestimates the ion conductivities of crystalline phases of an MLIP [20] as shown in Fig. 1. However, since the AIMD simulations of glass systems were conducted with a smaller number of ions, shorter time for annealing, quenching, equilibration, and calculating diffusion coefficient, and at higher temperatures, the deviation may also come from these conditions of MD simulation. Therefore, we believe that this deviation from the AIMD does not impact the validation of the present simulation and the relative difference in ion conductivity depending on the tensile strain is meaningful.

The effect of tensile strain is at most about 2× improvement in ion conductivity at RT in the case of strain increase from 0 to +2%. This is consistent with an AIMD result [16] where the ion conductivity is approximately 3× improved by 3% strain. This strain effect can explain the increase in ion conductivity observed in Ref. [11] at very low crystallinity ($7.5 \times 10^{-4}\,\mathrm{S\,cm^{-1}}$ at RT, yellow triangle in Fig. 6d), which is about 1.25× improvement from zero crystallinity ($5.9 \times 10^{-4}\,\mathrm{S\,cm^{-1}}$, yellow circle in Fig. 6d). Furthermore, the increase in ion conductivity in Ref. [11] occurred even when the nucleated crystalline phase was not a high ion-conducting phase, which is consistent with the present study where the crystal inside the glass is low ion-conducting γ-phase. The current study suggests that by nucleating high-density nano-crystals—which are not necessarily high ion-conducting phases—tensile strain distribution in glass matrix could enhance the ion conductivity of Li_3PS_4 glass-ceramics.

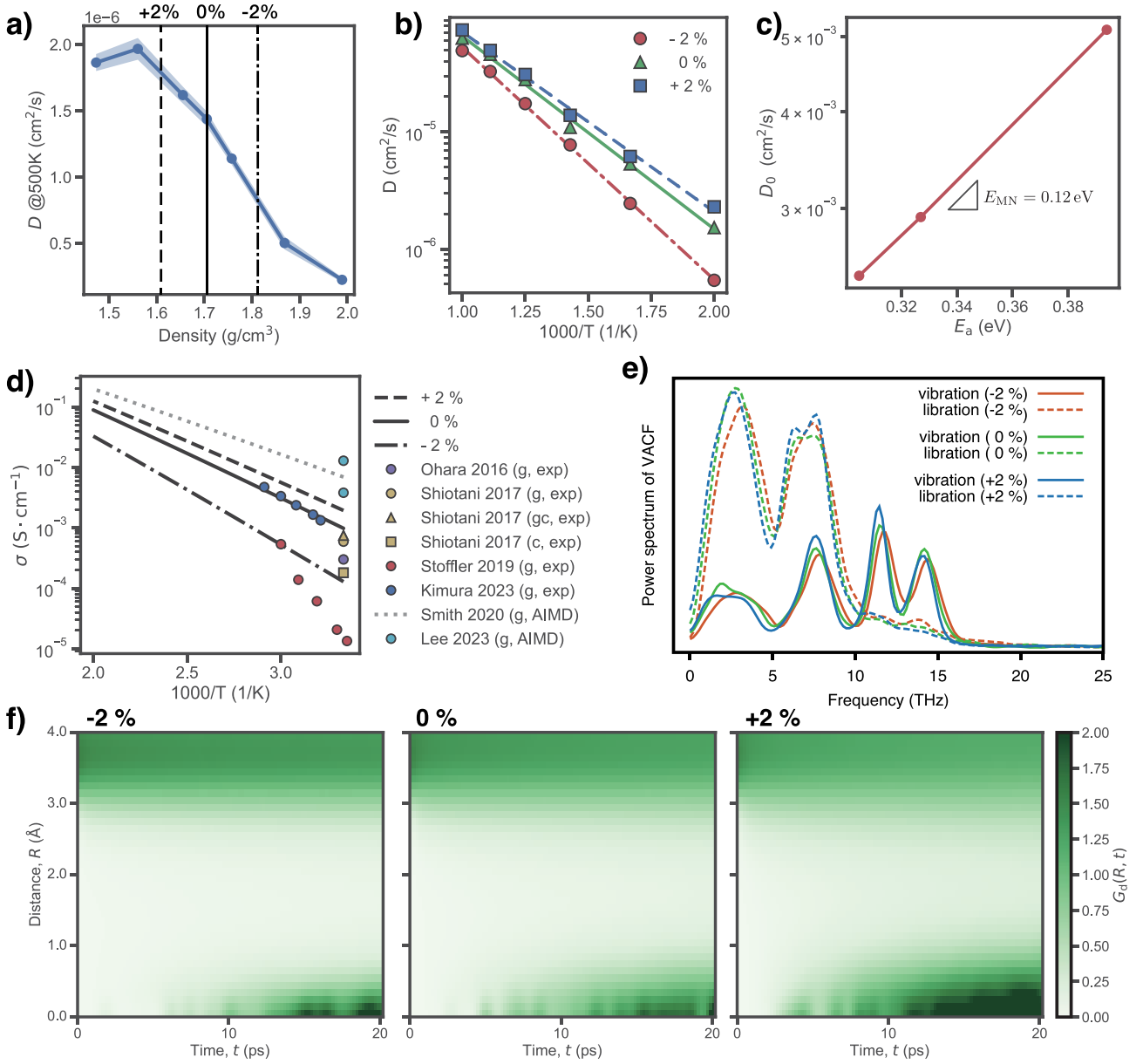

Fig. 6 Strain dependence of Li conductivity in Li_3PS_4 glasses. **a** Diffusion coefficient, D, of glass models at 500 K as a function of density. Shaded area shows error range estimated from 20 samples and densities of deformed systems (-2%, 0%, and +2%) are indicated with broken, solid, and dash-dot lines, respectively. **b** Arrhenius plot of D's; **c** the prefactor of the diffusion coefficient, D_0, as a function of the activation energy, E_a, of equilibrium glass model and strained (±2%) models. **d** Comparison of Li-ion conductivities obtained at (b) and those from the literature (Ohara 2016 [4], Shiotani 2017 [11], Stöffler 2019 [14], Kimura 2023 [10], Smith 2020 [19], and Lee 2023 [16]). Circles, triangles, and squares indicate glass (g), glass-ceramic (gc), and crystalline (c) phases, respectively. Two data from Lee 2023 (g, AIMD) are ionic conductivities of different densities, 1.8 g/cm^3 for a higher one and 2.0 g/cm^3 for a lower one. **e** The phonon DOS of vibration and libration modes of PS_4 units and **f** the distinct part of the van Hove correlation function of Li-ions, $G_d(\boldsymbol{r}, t)$, of the strained glass models

To further investigate the influence of the strain on the dynamical properties of strained glass systems, we computed the phonon density of states (DOS) of vibrational and librational motions of PS_4 units and plotted in Fig. 6(e). Overall shapes of vibrational and librational spectra are the same for the strained systems, except that the spectra slightly shift toward lower frequency as the system size increases and the density decreases. We also computed the distinct part of van Hove correlation function, $G_d(\boldsymbol{r}, t)$, of the strained systems as shown in Fig. 6(f). The van Hove correlation at zero distance,

$r = 0$, provides the information of possibility (at time t) of neighboring j-th Li-ion coming to the position where i-th Li-ion exists at $t = 0$, indicating the presence of correlations between neighboring Li-ions. By looking at $G_d(0, t)$ of the tensile (+2%) and compressed (-2%) systems in Fig. 6(f), the neighboring j-th Li-ions come to $\boldsymbol{r} = 0$ approximately 2x earlier in the tensile system ($\sim$ 5 ps) than in the compressed system ($\sim$ 10 ps). Consequently, although the influence of the strain on the dynamical properties of PS_4 units is minor, the correlation between Li-ions is influenced remarkably, resulting in the change in the activation energy E_a (Fig. 6b) and the prefactor D_0 (Fig. 6c).

Conclusions

A large-scale MD simulation of glass Li_3PS_4 with a γ-phase nano-crystal reveals that there appears a tensile strain field surrounding the nano-crystal because of the difference in equilibrium densities of glass and crystal phases. Furthermore, the MD simulation validates the glasses' increased ionic conductivity and decreased activation energy under tensile strain. These findings suggest that even in cases where the nucleated crystalline phase is not a high-conductivity phase and the crystalline regions do not percolate, the inhomogeneous tensile strain field increases the ion conductivity of the entire glass-ceramic Li_3PS_4. This discovery raises the prospect of enhancing the ion conductivity of glass-ceramic materials through regulation of the nano-crystal dispersion and crystallinity. Further research is needed to explore the quantitative relationship between increased ionic conductivity and crystallinity, which necessitates examining nano-crystal distribution on a larger length scale and strain relaxation within the glass matrix over an extended time frame that are challenges beyond the scope of current MD simulations.

Methods

Interatomic potential (IP) function form

We employed the IP developed in Ref. [23] that is composed of Coulomb repulsion between cation-cation and anion-anion, Morse potential between cation-anion, and angular potential between selected bonds as

$$U = \sum_i \sum_{j>i} \left[s\tilde{\phi}^{\mathrm{Coul}}(r_{ij}) + \tilde{\phi}^{\mathrm{Morse}}(r_{ij}) \right] + \sum_{(i,j,k)} \phi^{\mathrm{angular}}(\boldsymbol{r}_{ij}, \boldsymbol{r}_{ik}), \tag{1}$$

where $\tilde{\phi}(r)$ is the smoothed cutoff function of $\phi(r)$ defined as $\tilde{\phi}(r) = \phi(r) - \phi(r_c) - (r - r_c)\phi'(r_c)$ with cutoff radius r_c, and s is the scaling factor for the Coulomb potential. The Coulomb potential has the form of screened Coulomb using the complementary error function as

$$\phi^{\mathrm{Coul}}(r_{ij}) = k\frac{q_i q_j}{r_{ij}} \mathrm{erfc}\left(\frac{r_{ij}}{d_{ij}}\right), \tag{2}$$

where q_i and q_j are charges of ions i and j, respectively. The formal charges–−1.0, 5.0, and −2.0 for Li, P, and S, respectively—were used in the current IP. d_{ij} is the screening length, which is defined as a sum of effective radii of ions, $d_{ij} = d_i + d_j$. k is the prefactor to convert the unit containing the vacuum permittivity. The Morse potential is defined as

$$\phi^{\mathrm{Morse}}(r_{ij}) = D_{ij}\left\{\exp[-2\alpha_{ij}(r_{ij} - s_{ij})] - 2\exp[-\alpha_{ij}(r_{ij} - s_{ij})]\right\}, \tag{3}$$

where D_{ij}, α_{ij}, s_{ij} are the optimizing parameters between interacting pair i-j. The angular potential form was slightly modified from that introduced in Ref. [23, 24] as

$$\phi^{\mathrm{angular}}(\boldsymbol{r}_{ij}, \boldsymbol{r}_{jk}) = \lambda_{ijk} \exp\left[(r_{ij} - r_c^{3b})^{-1} + (r_{ik} - r_c^{3b})^{-1}\right] \left[(\cos\theta_{ijk} - \gamma_{ijk})^2 + \eta_{ijk}\right], \tag{4}$$

where $\lambda_{ijk}, \gamma_{ijk}, \eta_{ijk}$ are the optimizing parameters for the angle between two bonds, i-j and i-k, and r_c^{3b} is the cutoff radius for the 3-body angular potential. The parameter η_{ijk} was introduced to raise the potential energy when the bond j-i-k is formed regardless of its angle.

The Coulomb repulsions work between Li-Li, P-P, S-S, and Li-S and the Morse potentials on Li-S and P-S. The original angular potentials ($\eta_{ijk} = 0$) were applied to P-S-S and S-P-Li (in the order of i-j-k), and the modified angular ($\eta_{ijk} > 0$) was applied to S-P-P to hinder clustering of PS_4 units.

The optimized parameters and bulk properties of Li_3PS_4 are summarized in Supplementary Information.

Ab-initio calculations

Ab-initio calculations based on the density functional theory (DFT) were used to generate reference data for the optimization of IP. We performed the DFT calculations with the *Vienna ab-initio simulation package* (VASP) [25] using the projector-augmented wave method for pseudo-potentials [26] and the Perdew-Burke-Ernzerhof (PBE) generallized gradient approximation for the exhange-correlation functional [27]. Electron wave functions were represented by using a plane-wave basis set with an energy cutoff of 400 eV, and a reciprocal space was discretized with 15,000 k-points per $Å^{-1}$.

Pair distribution function (PDF)

The partial pair distribution function (p-PDF), $g_{\alpha\beta}(r)$, between two species α and β, and the total neutron-weighted PDF, $G(r)$, are widely used measures of the local structures of glasses and liquids [19]. They are defined as

$$g_{\alpha\beta}(r) = \frac{n_{\alpha\beta}(r)}{4\pi r^2 \mathrm{d}r \rho_\beta}, \tag{5}$$

$$G(r) = \sum_\alpha \sum_\beta \frac{c_\alpha c_\beta \bar{b}_\alpha \bar{b}_\beta}{\langle b \rangle^2} g_{\alpha\beta}(r), \tag{6}$$

where $n_{\alpha\beta}(r)$ is the number of β-species atoms at a distance between r and $r + \mathrm{d}r$ from the central α-species atom, ρ_β is the number density of species β, c_α is the fraction of the species α, $\bar{b}_\alpha$ is the neutron-scattering length of species α, and $\langle b \rangle = \sum_\alpha c_\alpha \bar{b}_\alpha$.

Construction of glass-ceramics model

The glass-ceramic Li_3PS_4 models of both 3D and pseudo-2D were created via the following procedure:

1. By duplicating a crystalline unit cell, create a nearly cubic crystalline structure with approximately 180 Å on each edge.
2. Anneal the system with variable cell vectors subject to constant volume at 1500 K for 100 ps, keeping the atoms inside the radius R_c fixed at their crystalline locations. To prevent certain bonds in PS_4 units from breaking, we modified Morse potential form of the P-S pair as a linear spring with a spring constant consistent with the Morse potential.
3. Quench the system with varying cell vectors under constant volume conditions from 1500 to 500 K so that the system requires a density of $\rho_g^* = 1.705\ \mathrm{g/cm^3}$.
4. Equilibrate the system at 500 K using an unaltered Morse potential and variable cell vectors subject to constant volume in which every atom is mobile, even within the radius R_c.

The density ρ_g^* is the equilibrium density of the glass formed by annealing up to 1500 K and quenching down to 500 K under 1 GPa with $N\sigma T$-MD using the current IP.

Local ion flux analysis from non-equilibrium MD

The local ion flux, $\boldsymbol{J}$, was evaluated from the non-equilibrium MD (NEMD) developed in Ref. [28]. In the NEMD, only the mobile ions (Li-ions in this case) were accelerated by an external force $\boldsymbol{F}^{\mathrm{ext}}$ and the velocities of other ions were corrected so that their total momenta became zero for the system not to have a translational velocity. The local ion flux in a local region was computed from the average velocities of particles over time inside the local region. The strength of the external force was chosen as $|\boldsymbol{F}^{\mathrm{ext}}| = 0.02\ \mathrm{eV/Å}$, which is small enough so that the ion mobility can be obtained in linear response assumption. The ion mobility can be computed from calculated ion flux as $\mu = |\boldsymbol{J}|/(n|\boldsymbol{F}^{\mathrm{ext}}|)$, where n is the number density of Li-ion.

Ion conductivity calculation using MD

The diffusion coefficient D of Li-ion was computed from the slope of the mean square displacement (MSD) of Li-ions against time from the constant-cell and constant-temperature (NVT) MD. The slope was evaluated at the time domain where log-log plot of MSD vs. time is on a linear function [29]. Once D's are obtained for various temperatures, the activation energy E_a can be evaluated from the slope of the Arrhenius plot, $\ln(D)$ vs. $1/T$, with $D(T) = D_0 \exp(-E_a/k_B T)$. The prefactor, D_0, may also be related to E_a as $D_0 \propto \exp(E_a/E_{MN})$, which is known as the Meyer-Neldel rule [30] and E_{MN} is a parameter that can be determined from the slope of the plot, $\ln(D_0)$ vs. E_a. The ion conductivity at a certain temperature, T, was computed via the Nernst-Einstein relation using $D(T)$ as

$$\sigma(T) = \frac{nq^2}{k_B T} D(T), \tag{7}$$

where q is the charge of Li-ion, and k_B the Boltzmann constant. Furthermore, the ion conductivity at lower temperatures than the MD simulations was obtained by extrapolating the Eq. (7) using $D(T)$. Note that $\sigma(T)$ is not a DC ionic conductivity since D does not include an interparticle correlation effect [31, 32].

Van Hove correlation function

The van Hove correlation function of Li-ions is defined as [33],

$$\begin{aligned} G(\boldsymbol{r}, t) &= \frac{1}{N} \sum_{i=1}^{N} \left[\frac{1}{\Omega_r} \sum_{j=1}^{N} \delta(\boldsymbol{r} + \boldsymbol{r}_i(0) - \boldsymbol{r}_j(t)) \right] \\ &= \left\langle \sum_{j=1}^{N} \delta(\boldsymbol{r} + \boldsymbol{r}_i(0) + \boldsymbol{r}_j(t)) \right\rangle, \end{aligned} \tag{8}$$

where the sum is taken over Li-ions and Ω_r is the volume of the shell at radius r. $G(\boldsymbol{r}, t)$ can be divided into the self part ($i = j$) and distinct part ($i \neq j$) as

$$\begin{aligned} G(\boldsymbol{r}, t) &= \langle \delta(\boldsymbol{r} + \boldsymbol{r}_i(0) - \boldsymbol{r}(t)) \rangle + \left\langle \sum_{j \neq i}^{N} \delta(\boldsymbol{r} + \boldsymbol{r}_i(0) - \boldsymbol{r}_j(t)) \right\rangle \\ &\equiv G_s(\boldsymbol{r}, t) + G_d(\boldsymbol{r}, t). \end{aligned} \tag{9}$$

The distinct part $G_d(\boldsymbol{r}, t)$ shows the possibility of other ions ($j \neq i$) coming to the position of ion-i at time $t = 0$ and thus it is used to investigate the correlation between Li-ions.

Phonon density of states (DOS)

The phonon DOS is computed as the Fourier transformation of velocity autocorrelation (VAC). The VAC can be computed as

$$Z(t) = \frac{\langle \boldsymbol{v}_i(t) \cdot \boldsymbol{v}_i(0) \rangle}{\langle \boldsymbol{v}_i(0) \cdot \boldsymbol{v}_i(0) \rangle}, \tag{10}$$

where $\boldsymbol{v}_i(t)$ is the velocity of an atom-i at time t. The VACs of vibrational and librational contributions of PS_4 units can be computed using velocities of S-ions and related unit P-S bond vectors $\boldsymbol{\tau}^{\mathrm{PS}}$ as

$$\boldsymbol{v}_i^{\mathrm{vib}}(t) = (\boldsymbol{v}_i(t) \cdot \boldsymbol{\tau}_i^{\mathrm{PS}})\boldsymbol{\tau}_i^{\mathrm{PS}}, \quad \boldsymbol{v}_i^{\mathrm{lib}}(t) = \boldsymbol{v}_i(t) - \boldsymbol{v}_i^{\mathrm{vib}}(t). \tag{11}$$

Supplementary Information The online version contains supplementary material available at https://doi.org/10.1007/s10008-024-05892-9.

Acknowledgements This work was supported by the JSPS KAKENHI Grant Numbers 21K04650 and 22H04613 (Grant-in-AId for Scientific Research on Innovative Areas "Interface Ionics"), and funded by Murata Manufacturing Co., Ltd. The computations were carried out using the supercomputers at the Information Technology Center, Nagoya University, the Institute for Solid State Physics, the University of Tokyo, and the Research Institute for Information Technology, Kyushu University. We used Ovito [34] for the visualization of atomic structures and ion flux distributions. RK would like to thank Dr. Kazutaka Ikeda at J-PARC CROSS, Prof. Koji Ohara at Shimane Univ., Prof. Shigeo Mori and Prof. Akitoshi Hayashi at Osaka Metropolitan Univ. for fruitful discussion.

Author contribution Ryo Kobayashi: conceptualization, methodology, investigation, writing—original draft, reviewing, and editing. Seiji Takemoto: validation, writing—reviewing and editing. Ryuichiro Ito: investigation.

Funding Open Access funding provided by Nagoya Institute of Technology. This work was supported by the JSPS KAKENHI Grant Numbers 21K04650 and 22H04613 (Grant-in-AId for Scientific Research on Innovative Areas "Interface Ionics"), and funded by Murata Manufacturing Co., Ltd.

Data availablility The source codes used to optimize the potential parameters and to conduct MD and NEMD simulation are available at https://github.com/ryokbys/optzer and https://github.com/ryokbys/nap, respectively. The input files and jupyter notebooks used in this study can be availed from the corresponding author upon reasonable request

Declarations

Generative AI and AI-assisted technologies in the writing process During the preparation of this paper, the authors used QuillBot (https://quillbot.com/) in order to improve readability and language. After using these services, the authors reviewed and edited the content as needed and take full responsibility for the content of the publication.

Conflict of interest The authors declare no competing interests.

References

1. Famprikis T, Canepa P, Dawson JA, Islam MS, Masquelier C (2019) Fundamentals of inorganic solid-state electrolytes for batteries. Nat Mater. https://doi.org/10.1038/s41563-019-0431-3
2. Nakayama M, Nakano K, Harada M, Tanibata N, Takeda H, Noda Y, Kobayashi R, Karasuyama M, Takeuchi I, Kotobuki M (2022) Na superionic conductor-type LiZr2(PO4)3 as a promising solid electrolyte for use in all-solid-state li metal batteries. Chem Commun 58(67):9328–9340. https://doi.org/10.1039/D2CC01526A
3. Cao C, Li Z-B, Wang X-L, Zhao X-B, Han W-Q (2014) Recent advances in inorganic solid electrolytes for lithium batteries. Front Energy Res 2:25. https://doi.org/10.3389/fenrg.2014.00025
4. Ohara K, Mitsui A, Mori M, Onodera Y, Shiotani S, Koyama Y, Orikasa Y, Murakami M, Shimoda K, Mori K, Fukunaga T, Aai H, Uchimoto Y, Ogumi Z (2016) Structural and electronic features of binary li_2s-p_2s_5 glasses. Sci Rep 6:21302. https://doi.org/10.1038/srep21302
5. Dietrich C, Weber DA, Sedlmaier SJ, Indris S, Culver SP, Walter D, Janek J, Zeier WG (2017) Lithium ion conductivity in Li2S–P2S5 glasses – building units and local structure evolution during the crystallization of superionic conductors Li3PS4, Li7P3S11 and Li4P2S7. J Mater Chem A Mater Energy Sustain 5(34):18111–18119. https://doi.org/10.1039/C7TA06067J
6. Homma K, Yonemura M, Kobayashi T, Nagao M, Hirayama M, Kanno R (2011) Crystal structure and phase transitions of the lithium ionic conductor Li3PS4. Solid State Ionics 182(1):53–58. https://doi.org/10.1016/j.ssi.2010.10.001
7. Liu Z, Fu W, Payzant EA, Yu X, Wu Z, Dudney NJ, Kiggans J, Hong K, Rondinone AJ, Liang C (2013) Anomalous high ionic conductivity of nanoporous β-Li3PS4. J Am Chem Soc 135(3):975–978. https://doi.org/10.1021/ja3110895
8. Sakuda A, Hayashi A, Tatsumisago M (2013) Sulfide solid electrolyte with favorable mechanical property for all-solid-state lithium battery. Sci Rep 3:2261. https://doi.org/10.1038/srep02261
9. Kim J-S, Jung WD, Choi S, Son J-W, Kim B-K, Lee J-H, Kim H (2018) Thermally induced S-sublattice transition of Li3PS4 for fast lithium-ion conduction. J Phys Chem Lett 9(18):5592–5597. https://doi.org/10.1021/acs.jpclett.8b01989
10. Kimura T, Inaoka T, Izawa R, Nakano T, Hotehama C, Sakuda A, Tatsumisago M, Hayashi A (2023) Stabilizing high-temperature α-Li3PS4 by rapidly heating the glass. J Am Chem Soc 145(26):14466–14474. https://doi.org/10.1021/jacs.3c03827

11. Shiotani S, Ohara K, Tsukasaki H, Mori S, Kanno R (2017) Pair distribution function analysis of sulfide glassy electrolytes for all-solid-state batteries: understanding the improvement of ionic conductivity under annealing condition. Sci Rep 7(1):6972. https://doi.org/10.1038/s41598-017-07086-y
12. Kim J-S, Jung WD, Son J-W, Lee J-H, Kim B-K, Chung K-Y, Jung H-G, Kim H (2019) Atomistic assessments of lithium-ion conduction behavior in glass-ceramic lithium thiophosphates. ACS Appl. Mater. Interfaces 11(1):13–18. https://doi.org/10.1021/acsami.8b17524
13. Wang Y, Richards WD, Ong SP, Miara LJ, Kim JC, Mo Y, Ceder G (2015) Design principles for solid-state lithium superionic conductors. Nat Mater 14(10):1026–1031. https://doi.org/10.1038/nmat4369
14. Stöffler H, Zinkevich T, Yavuz M, Hansen A-L, Knapp M, Bednarčík J, Randau S, Richter FH, Janek J, Ehrenberg H, Indris S (2019) Amorphous versus crystalline li_3ps_4: local structural changes during synthesis and li ion mobility. J Phys Chem C 123(16):10280–10290. https://doi.org/10.1021/acs.jpcc.9b01425
15. Yamada H, Ohara K, Hiroi S, Sakuda A, Ikeda K, Ohkubo T, Nakada K, Tsukasaki H, Nakajima H, Temleitner L, Pusztai L, Ariga S, Matsuo A, Ding J, Nakano T, Kimura T, Kobayashi R, Usuki T, Tahara S, Amezawa K, Tateyama Y, Mori S, Hayashi A (2023) Lithium ion transport environment by molecular vibrations in ion-conducting glasses. Energy Environ Mater. https://doi.org/10.1002/eem2.12612
16. Lee B, Jun K, Ouyang B, Ceder G (2023) Weak correlation between the polyanion environment and ionic conductivity in amorphous Li-P-S superionic conductors. Chem Mater 35(3):891–899. https://doi.org/10.1021/acs.chemmater.2c02458
17. Lundén A (1988) Evidence for and against the paddle-wheel mechanism of ion transport in superionic sulphate phases. Solid State Commun 65(10):1237–1240. https://doi.org/10.1016/0038-1098(88)90930-1
18. Jansen M (1991) Volume effect or paddle-wheel mechanism–fast alkali-metal ionic conduction in solids with rotationally disordered complex anions. Angew Chem Int Ed Engl 30(12):1547–1558. https://doi.org/10.1002/anie.199115471
19. Smith JG, Siegel DJ (2020) Low-temperature paddlewheel effect in glassy solid electrolytes. Nat Commun 11(1):1483. https://doi.org/10.1038/s41467-020-15245-5
20. Gigli L, Tisi D, Grasselli F, Ceriotti M (2023) Mechanism of charge transport in lithium thiophosphate. arXiv:2310.15679 [cond-mat.mtrl-sci]
21. Shimizu K, Bahuguna P, Mori S, Hayashi A, Watanabe S (2023) Enhanced ionic conductivity through crystallization of glass-Li_3PS_4 by machine learning molecular dynamics simulations. arXiv [cond-mat.mtrl-sci]. arXiv:2312.06963 [cond-mat.mtrl-sci]
22. Yang X-S, Deb S (2009) Cuckoo search via levy flights, 210–214. https://doi.org/10.1109/NABIC.2009.5393690
23. Kobayashi R, Miyaji Y, Nakano K, Nakayama M (2020) High-throughput production of force-fields for solid-state electrolyte materials. APL Mater 8(8):081111. https://doi.org/10.1063/5.0015373
24. Stillinger FH, Weber TA (1985) Computer simulation of local order in condensed phases of silicon. Phys Rev B Condens Matter Mater Phys 31(8):5262–5271. https://doi.org/10.1103/PhysRevB.31.5262
25. Kresse G, Furthmüller J (1996) Efficient iterative schemes for ab initio total-energy calculations using a plane-wave basis set. Phys Rev B Condens Matter 54(16):11169–11186. https://doi.org/10.1103/physrevb.54.11169
26. Blöchl PE (1994) Projector augmented-wave method. Phys Rev B Condens Matter 50(24):17953–17979. https://doi.org/10.1103/physrevb.50.17953
27. Perdew JP, Burke K, Ernzerhof M (1996) Generalized gradient approximation made simple. Phys Rev Lett 77(18):3865–3868
28. Kobayashi R, Nakano K, Nakayama M (2022) Non-equilibrium molecular dynamics study on atomistic origin of grain boundary resistivity in NASICON-type li-ion conductor. Acta Mater 226:117596. https://doi.org/10.1016/j.actamat.2021.117596
29. Maginn EJ, Messerly RA, Carlson DJ, Roe DR, Richard Elliot J (2019) Best practices for computing transport properties 1. Self-Diffusivity and viscosity from equilibrium molecular dynamics [article v1.0]. Living J Comp Mol Sci 1(1):6324–6324. https://doi.org/10.33011/livecoms.1.1.6324
30. Takamure N, Sun X, Nagata T, Ho-Baillie A, Fukata N, McKenzie DR (2022) Thermodynamic interpretation of the Meyer-Neldel rule explains temperature dependence of ion diffusion in silicate glass. Phys. Rev. Lett. 129(17):175901. https://doi.org/10.1103/PhysRevLett.129.175901
31. Murch GE (1982) The haven ratio in fast ionic conductors. Solid State Ionics 7(3):177–198
32. Marcolongo A, Marzari N (2017) Ionic correlations and failure of Nernst-Einstein relation in solid-state electrolytes. Phys Rev Materials 1(2):025402. https://doi.org/10.1103/PhysRevMaterials.1.025402
33. Hansen JP, McDonald IR (1990) Theory of simple liquids. Elsevier Science. https://books.google.co.jp/books?id=1lOtRVQMYuIC
34. Stukowski A (2009) Visualization and analysis of atomistic simulation data with OVITO-the open visualization tool. Modell Simul Mater Sci Eng 18(1):015012. https://doi.org/10.1088/0965-0393/18/1/015012